V_P Structure of Mount St. Helens, Washington, USA, Imaged with Local Earthquake Tomography

Gregory P. Waite[a,1] and Seth C. Moran[b]

[a] US Geological Survey, 345 Middlefield Rd., Menlo Park, CA 94025, USA
[b] US Geological Survey, 1300 SE Cardinal Ct., Bldg. 10, Ste. 100, Vancouver, WA 98683, USA
[1] now at Dept. of Geol. & Mining Eng. & Sciences, Michigan Technological University, 1400 Townsend Dr., Houghton, MI 49931, USA

corresponding author:
Dept. of Geol. & Mining Eng. & Sciences
Michigan Technological University,
1400 Townsend Dr.
Houghton, MI 49931, USA
tel: 011-906-487-3554
fax: 011-906-487-3371
gpwaite@mtu.edu

Abstract.

We developed a new *P*-wave velocity model for Mount St. Helens using local earthquake data recorded by the Pacific Northwest Seismograph Stations and Cascades Volcano Observatory since the 18 May 1980 eruption. These data were augmented with records from a dense array of 19 temporary stations deployed during the second half of 2005. Because the distribution of earthquakes in the study area is concentrated beneath the volcano and within two nearly linear trends, we used a graded inversion scheme to compute a coarse-grid model that focused on the regional structure, followed by a fine-grid inversion to improve spatial resolution directly beneath the volcanic edifice. The coarse-grid model results are largely consistent with earlier geophysical studies of the area: we find high-velocity anomalies NW and NE of the edifice that correspond with igneous intrusions and a prominent low-velocity zone NNW of the edifice that corresponds with the linear zone of high seismicity known as the St. Helens Seismic Zone. This low-velocity zone may continue past Mount St. Helens to the south at depths below 5 km. Directly beneath the edifice, the fine-grid model images a low-velocity zone between about 2 and 3.5 km below sea level that may correspond to a shallow magma storage zone. And although the model resolution is poor below about 6 km, we found low velocities that correspond with the aseismic zone between about 5.5 and 8 km that has previously been modeled as the location of a large magma storage volume.

1. Introduction

Mount St. Helens (MSH) is a stratovolcano located in southwestern Washington State within the Cascades magmatic arc. The 300,000 year eruption history of MSH (Clynne *et al.*, 2008) includes the most recent eruptive cycle that began in spring 1980 and culminated in the 18 May 1980 explosive eruption. This was followed by 6 years of dome-building eruptions and, after an 18-year pause, additional dome building in 2004-2008.

The unrest leading up to the 18 May 1980 eruption prompted detailed geological and geophysical studies of the volcano, which included the installation of an improved earthquake-monitoring network that continues operating today. Studies made using these earthquake data have revealed details about the tectonic setting (e.g., Weaver *et al.*, 1987), spatial and temporal variations in the stress field (Barker and Malone, 1991; Moran, 1994), the structure of the magmatic plumbing system (Musumeci *et al.*, 2002) and the subsurface velocity structure (Lees, 1992; Moran *et al.*, 1999).

Regional seismic tomography studies (Lees and Crosson, 1989; Lees and Crosson, 1990; Moran *et al.*, 1999) have consistently imaged several large-scale features in the mid to upper crust that correlate with geological structures and geophysical anomalies in the region surrounding MSH. The most notable of these are: 1) a low-velocity zone that parallels a NNW trending zone of earthquakes, the St. Helens Seismic Zone (SHZ); and 2) high velocities beneath the Spirit Lake and Spud Mountain plutons north of MSH. Parsons *et al.* (1999) recorded active sources with a linear, E-W array about 40 km north of MSH. They found a sharp velocity decrease from west to east at depths below 10 km where the array crossed the SHZ. Lees (1992) imaged smaller-scale features beneath MSH, including prominent low-velocity zones that were interpreted as elements of the magmatic system. Lees (1992) also imaged a high-velocity anomaly between about 6 and 9 km

depth beneath the volcano that was interpreted as a plug of solidified magma on top of the main magma-rich volume.

In this study, we combined 25 years of network-recorded seismicity since the 18 May 1980 eruption with data from a temporary array of 19 broadband seismometers deployed from June 2005 through early 2006 to compute a new *P*-wave velocity model of the upper crust beneath MSH. The additional data, different inversion method (SIMULPS (Thurber, 1983; Eberhart-Phillips, 1990; Evans *et al.*, 1994)) together with the 3-D ray shooting method (Haslinger and Kissling, 2001) that we use, provide a somewhat different image of the velocity structure than was determined previously by Lees (1992).

2. Earthquake Data

The Pacific Northwest Seismic Network (PNSN), based out of the University of Washington, encompasses all of Oregon and Washington, including MSH. The network configuration has changed somewhat since 1980, but has always included about 10 stations within 10 km of the center of the volcano (Figure 1). Until 2004, these stations were all vertical-component, short-period stations. In June 2005 we augmented this network with a temporary 19-station array of broadband stations within 6 km of the volcano, with stations removed by July 2006 (Waite *et al.*, 2008).

Earthquakes near MSH are generally confined to a near-vertical, cylindrical volume directly beneath the edifice (Figure 2) and a band of epicenters that extends to the NNW and SSE of MSH that is known as the St. Helens Seismic Zone (SHZ) (Weaver and Smith, 1983). Focal mechanisms for events in this zone are consistent with right-lateral motion along the NNW trend of the SHZ (Weaver *et al.*, 1987). There are several concentrations of epicenters along a trend, which is approximately perpendicular to the SHZ, but this trend is less well defined. Focal mechanisms of

one event in each of the two clusters to the NE of MSH are the same style as those in the SHZ and are interpreted by Weaver *et al*. (1987) to be related to sets of faults that strike nearly parallel to the SHZ. The densest seismicity is directly beneath MSH to a depth of about 10 km. An earthquake-free zone beneath the volcano beginning at a depth of about 6 km has previously been postulated as the location of the main crustal magma body (e.g., Scandone and Malone, 1985).

Between June 1980 and the September 2004, 19,379 earthquakes were located by the PNSN within a 50 km by 50 km area centered on MSH. Because the shape of the volcano changed dramatically during the 18 May 1980 eruption, we only used data recorded following that event. An additional 6916 events were located in this area between October 2004 and the end of 2005, which represents a small fraction of the total number of events associated with the 2004-2008 eruption. The large number of earthquakes in the catalog permits a careful selection of data for only the best-quality events (Figure 2).

We restricted our dataset to include only well-located events according to the following criteria: 1) azimuthal station gap < 180º; 2) root mean square (RMS) residual in one-dimensional model less than or equal to 0.25 s; 3) at least 10 stations with 0, 1, or 2 analyst-assigned weight picks; and 4) a closest station with an epicentral distance less than or equal to the depth. Weights 0, 1, 2, 3, and 4 correspond to uncertainties <0.03, <0.06, <0.15, <0.30, and >0.30 s, respectively. The quality criteria reduced the number of useable events to 7798. To reduce the bias of the over-sampled region directly beneath the edifice, we initially imposed an additional restriction that no two earthquakes are within 250 m of each other. Data were sorted according to RMS residual, then selected so that this minimum spacing requirement was met.

3. Minimum 1-Dimensional Model

We derived a starting 1-D model that included P-wave velocities and station delays using the program Velest (Kissling *et al.*, 1994). Multiple iterations beginning with a range of staring velocity models were used to find a 1-D model that minimized the average rms residuals for all of the earthquakes in a 500-event subset. This process was repeated with an independent data set and the final, minimum 1-D model represents the best fit to both sets of earthquakes. The deepest layers were constrained by the regional crustal model of Parsons *et al*. (1999), which was derived from active-source and local earthquake data. The starting mid- to upper-crustal velocities were based on the 1-D model used for routine earthquake processing by the PNSN (UW-S3, Malone and Pavlis, 1983) and a modified version of UW-S3 (CVO2) defined for earthquakes directly beneath MSH (see Endo *et al*., 1990) that differs only in the slower shallowest layers. The layered starting models, final minimum 1-D model, and interpolated 3-D starting model are shown in Figure 3.

The complexities of topography and very-low velocities in the volcanic edifice made modeling the shallowest layers difficult. While we did account for topography in the ray tracing by forcing rays to stay below the surface, we found that velocities in the upper 3-5 km (i.e., from just below sea level to the highest elevations) were unstable and depended strongly on the data subset. As a result, we constrained our 1-D model to have higher velocities than the CVO2 model but lower than the UW-S3 model in the shallowest layers. The resultant minimum 1-D starting model ("velest" in Figure 3) has slightly lower velocities (~200 m/s) than the UW-S3 model nearly everywhere.

4. Coarse-Grid Inversion

4.1. Inversion procedure

All the earthquakes were relocated using the new 1-D model and station corrections, and solutions were re-examined for quality. We expanded the dataset to include events with a closest station up to 1.5 times the depth, but the other criteria were kept the same. Again, we sorted the data by RMS and selected the best set such that no two events were within 250 m of each other. This left 1159 earthquakes with 18,942 P wave arrival times, just 10% of which were assigned the lowest pick weight (corresponding to an uncertainty <0.3 s).

We modeled the 3-D velocity structure in two steps. First we conducted a coarse-grid inversion, with grid nodes spaced 5 km apart horizontally and 2 km apart vertically in the well-sampled parts of the model (layers of nodes were placed at -3.1 km -1.1, 0.9, 2.9, 4.9, 6.9, 9.9, 13.9, 18.9, and 32.9 km, with all depths relative to sea level). This model was then used as a starting model for a fine-grid inversion that was focused on the volume directly beneath MSH. We used the inversion code SIMULPS (Thurber, 1983; Eberhart-Phillips, 1990; Evans *et al.*, 1994) extended for full 3-D ray shooting (Haslinger and Kissling, 2001) to invert for velocity-model and hypocenter-location changes simultaneously. We also inverted for station corrections, as the station spacing was much smaller than the grid spacing in some areas of the model. We further modified the code to include the complex topography, so that no rays or earthquakes could be above the ground (Figure 4).

We smoothed the model using an offset-and-average approach (Evans and Zucca, 1988; Castaño, 2002; Waite *et al.*, 2006) so that the final coarse-grid model is the average of 25 (5 x 5 x 2 km) models computed on distinct grid nodes. We refer to these 5 x 5 x 2 km grids as "inversion grids" and the 1 x 1 x 2 km grid that is used to compute the average model as the "averaging grid". The center of each of the 25 individual inversion grids was shifted by 1 km laterally (east-west

and/or north-south) so that each averaging grid node was occupied by exactly one inversion grid node. Each model was then linearly interpolated to the averaging grid before averaging. In this way, each point in the average was covered by one inversion grid node and 24 interpolated points from the other models. This procedure damped the strongest anomalies somewhat, but made it possible to resolve features smaller than the 5 km inversion grid-node spacing. It also reduced the potential for artifacts related to grid node positions and provided a smooth starting 3-D model for the fine-grid inversion.

We evaluated the model quality using the diagonal and spread of the model resolution matrix as well as inversions of synthetic anomalies. Checkerboard type tests and tests of synthetic anomalies with realistic shapes and sizes were also evaluated. Examples of one checkerboard test are shown in supplemental figure S01. The grid nodes plotted in Figure S01 are representative of a single model used in the inversions. In this example the starting anomalies had lateral extents of 6 km, slightly larger than the grid spacing. In addition, each anomaly was separated by 2 km laterally and in depth to highlight areas where tradeoff between neighboring anomalies is a problem. These gaps between anomalies were recovered in most cases. In the shallowest layers (-1.1 km and 0.9 km) the input anomalies were only recovered close to the edifice. The resolution improved below 0.9 km to ~6.9 km depth over an area ~10 km west and east of MSH, 10 km south and 15 km north. The diagonal elements of the resolution matrix and their spread confirmed the results of the synthetic inversions. At 9.9 km depth and below, the resolution is poor.

We assessed the trade-off between model and data variance to find an appropriate damping value. With a conservative damping value, we could recover up to 80% of the peak synthetic anomalies without excessive smearing between adjacent anomalies. Using damping of 200 s^2 for the velocity model and 400 for the station correction terms, the data variances of the 25 models were

reduced between 71.4% and 72.8% after 3 iterations and the RMS residuals were reduced from 0.122-0.125 s to 0.065-0.066 s.

We used the 25 individual models to estimate the uncertainty related to model parameterization. We computed the range of velocities at each point in the averaging grid and derived additional statistics from the ranges. A table of the maximum range and standard deviations of the ranges in each layer is given in supplementary Table 1. There are a small number of very large ranges in most layers, but the standard deviation of the ranges in each layer is low. The maximum range of 0.64 km/s (10.78%) is at 2.9 km depth, 7 km north and 10 km west of the center of the model at the edge of the high-velocity anomaly we interpret as the Spud Mountain Pluton (see the discussion below). The other points with large range values are near the Spud Mountain Pluton and the low-velocity zone that parallels the SHZ. The large values are a result of the interpolation between inversion grid nodes that lie within different anomalies. This layer has the largest standard deviation of ranges, 0.13 km/s (2.10%). The sharp contrast between these two anomalies also causes the largest range and standard deviation values in other layers. Only a small number of the averaging grid nodes have such large ranges in the 25 models. In the layer with the largest standard deviation (2.9 km), fewer than 25% of the points in a 40 km by 40 km area centered on the volcano have a range of values that exceeds 0.05 km/s; fewer than 3% of the points have ranges that exceed 0.10 km/s. The existence of the large velocity ranges adjacent to the sharp velocity contrasts highlights the utility of the offset-and-average procedure for resolving the edges of these anomalies.

4.2. Discussion of the coarse-grid inversion results

The key features of the coarse-grid model are high-velocity anomalies NW and NE of MSH and a low-velocity zone that extends to the NNW of MSH. These seismic velocity anomalies were imaged by previous seismic studies (Lees, 1992; Moran *et al.*, 1999), and the high-velocity

anomalies correspond with positive aeromagnetic anomalies (Finn and Williams, 1987). The Spirit Lake Pluton anomaly extends from near the surface to at least 4.9 km. It may extend deeper, but we could not resolve it in the deeper layers. This seismic anomaly extends farther to the south than the mapped extent of the Sprit Lake Pluton at the surface (Walsh *et al.*, 1987), but this was not unexpected given the widespread occurrence of contact metamorphic rocks in the area (Evarts *et al.*, 1987). The velocity of this anomaly at 4-6 km below the surface (~6.2 km/s) is consistent with granite at 5 km depth (e.g., Christensen and Mooney, 1995).

The fast velocity anomaly NW of MSH is likely due to an igneous intrusion as well. This feature was not mapped at the surface as a pluton, but has been inferred based on small isolated intrusions and contact metamorphism (Evarts and Ashley, 1990) near Spud Mountain. The positive aeromagnetic anomaly associated with this pluton extends north of the study area. Again, the velocities of this anomaly are consistent with a silicic intrusive body.

A low-velocity anomaly north and NNW of MSH correlates with the SHZ and a negative aeromagnetic anomaly (Finn and Williams, 1987). This negative aeromagnetic anomaly continues NNW and SSE of MSH parallel to the trend of prominent mapped contacts. This NNW trend also corresponds to the western extent of a conductive anomaly that encompasses the region between Mount Rainier, Mount Adams, and MSH (Stanley *et al.*, 1987). Previous studies have interpreted these features as a regional structural trend, such as a fault (e.g., Evarts *et al.*, 1987; Weaver *et al.*, 1987); the coincident velocity anomaly in our tomography results supports this idea.

South of MSH, our model resolution is limited to shallow depths and distances less than 5-10 km from MSH. A low-velocity anomaly to the SE is consistent with the same aeromagnetic and conductivity anomaly as the low-velocity anomaly NNW of MSH, and is likely part of the same regional structural feature. A weak high-velocity anomaly SW of MSH does not clearly correspond to surface features, but is consistent with a positive aeromagnetic anomaly that extends from MSH

to about 5 km SW (Finn and Williams, 1987). However, there is a strong trade-off between adjacent nodes that are SW of MSH due to a lack of crossing rays there, so this anomaly is not well resolved. We note that unlike the region north of MSH, the SHZ not well defined to the south. If a regional fault is responsible for the SHZ and velocity structure to the north, a wider fault zone may explain the more diffuse seismicity and less-well defined seismic velocity anomalies to the south of MSH.

5. Fine-grid Inversion

5.1. Inversion procedure

We used the smoothed coarse-grid results as a starting model for a fine (2 x 2 x 1 km) grid inversion that focused on the volume directly beneath MSH. The aim of this fine-grid modeling was to identify kilometer-scale elements of the MSH magmatic plumbing system. The inversion procedure we used was similar to that used for the coarse-grid modeling; we solved the coupled hypocenter-velocity model problem in the same way, but use more data. We again used an offset and averaging procedure, but the averaging grid had nodes spaced 500 m apart. We needed 16 models so that an inversion grid node occupied each node of the averaging grid. The 16 offset starting models were interpolated from the smoothed coarse-grid model with nodes at depths from -3.1 km by 1 km to 7.9 km, then 9.9, 13.9, 18.9, and 32.9 km.

We expanded the dataset for the fine-grid inversion by allowing events to be as close as 100 m. The other criteria were the same as in the coarse-grid modeling. Relaxing the event- spacing criterion created a dataset with 2973 earthquakes and 46,566 P-wave arrival times. Seventy-two percent of the arrivals were assigned a quality of either 0 or 1, corresponding to estimated uncertainties of < 60 ms. The data were relocated with the coarse-grid model and station corrections prior to the fine-grid inversions.

We reevaluated the damping parameter because of the increased number of model parameters (2672 compared with 1185) and data compared with the coarse-grid inversion, and found the optimal damping value was 20 s^2. The station correction damping was similarly re-evaluated and reduced to 100. While we inverted for station correction terms for each station, only the station correction parameters from stations at distances > 5 km from the volcano were carried over from the coarse inversion. All of the station correction terms within 5 km of the crater were reset to zero initially, but were free to vary during the inversions, so that more residual information could be mapped into the structure. The distance of 5 km was chosen because the densest seismicity was within this distance from the volcano and we expected to achieve the best resolution in the shallow part of the model in this region. Hypocenter locations were fixed for the first iteration. Resetting some station correction terms to zero and fixing the hypocenter locations had the effect of increasing the average RMS residual from ~0.066 s at the end of the coarse-grid inversions to ~0.078 s. After 3 iterations of fine-grid inversions, the RMS residual for the 16 models was reduced to values of 0.0568-0.572 s and the data variance reductions ranged from 46-47%.

The modified checkerboard tests in supplemental figure S2 and model resolution parameters in supplemental figure S3 demonstrate the inversion procedure's ability to resolve small-scale features directly beneath the volcano to a depth of ~7 km below sea level (bsl). Note that while there is significant smearing between adjacent nodes, the smeared anomalies typically represent only about 1% difference from the background velocity compared with +/-10% for the synthetic anomalies. The synthetic anomalies shown in Figure S2 are 4 x 4 x 1 km. As with the coarse-grid inversion, the anomalies are separated both horizontally and in depth to highlight areas with substantial tradeoff between neighboring anomalies. Figures S2 and S3 also illustrate the poor resolution at depths below 8 km and distances more than ~5 km from the volcano. In the inversions

using real data, the velocities in the poorly-resolved model space did not change significantly from the starting model velocities.

We interpolated the 16 2 x 2 x 1 km models to the 500 m spacing of the averaging grid and examined the statistics at the averaging grid nodes as we did for the coarse-grid models. As with the coarse-grid models, the largest ranges and standard deviations occurred at the boundaries of high-velocity Spud Mountain Pluton and low-velocity zone associated with the SHZ. Because of the finer inversion grid, the maximum ranges and standard deviations of the ranges at each node are typically lower than those of the corresponding locations in the coarse-grid models (supplementary table T2). The maximum range of 0.41 km/s (6.89%) is for a node at a depth of 2.9 km and the largest standard deviation of 0.06 km/s (1.29%) is in the layer at depth -0.1 km.

Because of the abundance of data, we were also able to examine models created with two independent data sets. Using the same procedure outlined above, apart from the offset-and-averaging, we computed fine-grid model A from 1541 earthquakes with 24,191 observations and fine-grid model B from 1526 earthquakes with 23,506 observations. The differences in the resulting models give an estimate of the absolute uncertainty in the velocities of the final model. The largest differences, as a percentage of the background velocity are 2.7% in layers at depths of -0.1 km and 7.9 km and 3.0% in the 9.9 km layer (supplementary table T3). The standard deviations are much smaller, less than or equal to 0.52% in all layers.

The differences between the individual fine-grid models calculated with identical data, but shifted grid locations, are much larger than the differences between the two models computed with identical parameterizations, but independent data. In the shallower layers (-1.1 to 5.9 km bsl) the maximum range of values in the shifted-grid models is 2 to 5 times larger than the difference between the two models derived from independent data. In this region, the parameterization has a larger impact on the model than the data.

5.2. Discussion of the fine-grid inversion results

The key features of the coarse-grid model are preserved in the fine-grid model. In addition, we imaged low velocities associated within the edifice, a low-velocity volume that lies beneath the crater at 1-3 km depth (3-5 km below the crater floor), and a prominent high-velocity volume at 3.5-6.5 km depth (5.5-7.5 km below the crater floor) just east of the zone of dense seismicity directly beneath the volcano (Figure 6).

We infer that the relatively low velocities in the edifice are related to poorly consolidated assemblages of debris, ash and lava flows. Resetting the station correction terms to 0 for stations on the edifice resulted in slightly lower velocities in the edifice than for inversions with initial correction terms derived from the coarse-grid inversion, but did not affect velocities below about 0 km depth. Directly beneath the edifice at ~0 km there is a thin region of high velocities. This feature may simply be due to the relatively greater depth that these rocks are found compared with rocks at sea level away from the edifice. The ~2 km of rock that overlies this zone is not found in areas where the topography is less than 1000 m above sea level and results in greater compaction, larger moduli, and higher seismic velocities.

The low-velocity volume at 1-3 km depth coincides with a similar feature found by Lees (1992) and may be related to a shallow magma storage volume, as proposed by Lees (1992). There is some evidence for a shallow magma reservoir (0 to 1 km bsl) from finite-element modeling of deformation data (Chadwick *et al.*, 1988). Bonaccorso and Davis (1999) modeled the same data using an analytical model of a thin, pressurized, vertical, prolate ellipsoid within a half-space, suggesting the deformation could have been due simply to pressurization in the conduit and not pressurization in a larger-scale magma chamber. Gas emission data can be explained by intrusion of a shallow magma reservoir (e.g., Casadevall *et al.*, 1983) prior to the 1980 eruption, but are not conclusive (Pallister *et al.*, 1992). Endo *et al.* (1990) also infer the existence of a shallow magma

chamber from about 500 m asl to 2.5 km bsl based on the distribution of earthquakes; a relatively aseismic zone between 1 and 2.5 km is interpreted as a magma-rich volume.

The low-velocity (-5.5%) volume at 1-3 km depth is consistent with the interpretation of Endo *et al.* (1990). While the true velocity anomaly may be lower than the modeled velocity, due to the effects of damping and infinite frequency approximation, laboratory (e.g., Murase and McBirney, 1973; Sato *et al.*, 1988) and analytical (e.g., Mavko, 1980; Hammond and Humphreys, 2000) work on the seismic velocities show that the percent compressional-wave velocity reduction is generally greater than or equal to the percent of partial melt. The relationship between seismic velocities and melt fraction is highly dependent on the geometry of the distributed melt (e.g., Hammond and Humphreys, 2000), but we might expect a small ~5% amount of melt to be responsible for the observed anomaly. Analyses of lavas from the eruption that began in 2004 indicate that magma could have been stored at depth of 2-3 km bsl for a relatively prolonged time (Rutherford and Devine, 2008), consistent with the depth of this shallow low-velocity body. Wiemer and McNutt (1997), who mapped *b*-values under MSH, found two anomalously high (~1.5) volumes at about 1-2 and 5.5 km bsl (Wiemer and McNutt (1997) reported depths relative to the crater floor, which is about 1.9 km asl). They interpret these regions as magma vesiculation and magma-rich zones, respectively, an analysis that is consistent with our tomographic model.

A significant difference between the model of Lees (1992) and our model is in the position of the high-velocity anomaly at 3.5-6.5 km depth. This anomaly is shifted about 1 km east and 1 km shallower in our model compared with the model of Lees (1992). Instead of lying within the zone of dense seismicity directly under the crater as it does in the model of Lees (1992), the high velocity anomaly is east of this zone of earthquakes. This is an important difference, because of the implications for interpreting the extent of magmatic system. Lees (1992) suggested that the anomaly is due to a plug of solidified magma at the top of a magma body, but this depth for the top of the

magma body is deeper than other models by 2-3 km (e.g., Scandone and Malone, 1985; Pallister *et al.*, 1992; Moran, 1994; Pallister *et al.*, 2008).

There are several possible explanations for the differences between the model of Lees (1992) and our model that relate, in part, to advances in tomographic imaging techniques during the 15 years that separate the two studies. We used different model parameterizations (2 x 2 x 1 km node spacing versus constant velocity blocks 0.5 km on a side) and different ray tracing techniques. We also used three-dimensional station locations plus a digital elevation model to ensure that rays stayed below the surface, while Lees (1992) did not take elevation into account except through station delays. This difference in datum might explain any discrepancy between the vertical positions of anomalies. Finally, we also used different data, although our test with a dataset that was similar to that used by Lees (1992) showed that the use of different data alone was not responsible for the differences between our two models.

A disadvantage of using the offset-and-average smoothing technique is that it moderates small anomalies that may represent important structural elements. In particular, the fine-grid model with nodes centered on the crater has a distinct low-velocity anomaly within the earthquake-free zone from 5-7 km bsl. This may represent a wide part of the magmatic conduit where magma was stored, but the strength of this low-velocity anomaly is reduced by the multimodel-smoothing procedure. The depth and position of the low velocity anomaly within the earthquake-free zone are consistent the location of a magma-storage volume suggested by previous seismic and petrologic studies (e.g., Scandone and Malone, 1985; Pallister *et al.*, 1992; Moran, 1994; Pallister *et al.*, 2008).

In order to highlight the low-velocity anomalies thought to be related to the magmatic system, we present an interpretive model based on a single fine-grid inversion in Figure 7. Grid nodes positioned directly beneath the volcano highlight the major features of the model: a shallow low-velocity zone that may be a shallow magma storage zone; the deeper low-velocity zone that

corresponds with the aseismic zone at about 5.5 km bsl; and relatively high-velocity material to the east of the magmatic conduit that may represent igneous intrusive rocks, such as gabbroic metamorphic inclusions found in the 1980-1986 and 2004-2006 lavas (Pallister *et al*., 2008).

6. Conclusions

The well-resolved velocity anomalies below MSH are generally consistent with previous studies that have found two igneous intrusive bodies NE and NW of the edifice, and a structural boundary that parallels the SHZ. North of MSH, the SHZ is bounded by a low-velocity anomaly to the west and the Spirit Lake Pluton to the east. The coincidence of the velocity anomalies and the trend of earthquakes strengthens the argument that MSH sits along a significant NNW-trending structural anomaly (e.g., Parsons *et al*., 1999).

Small-scale features of the magmatic system were less well resolved, but a significant low-velocity zone from 1-3 km bsl may be due to a shallow magma-storage reservoir. A strong high-velocity anomaly, previously interpreted as a magma plug (Lees, 1992) was found to be east of the vertical zone of earthquakes directly beneath MSH instead of within the earthquake zone. This anomaly may be attributed to crystallized magma, but we do not interpret it as a plug within the conduit. The deeper low-velocity anomaly that we interpret as part of the magma storage system is poorly resolved due to the lack of deep earthquakes, but is consistent with earlier suggestions that the earthquake-free region is likely to be magma rich.

7. Acknowledgments

This work benefited from productive discussions with Jonathan Lees and scientists at CVO and USGS Menlo Park especially John Pallister and Mike Clynne. Thanks to John Power and Phil Dawson for constructive reviews. We thank the staff at the PNSN for their dedication to providing high-quality data and IRIS-PASSCAL Instrument Center for providing instruments and support for

the temporary network. Data collected will be available through the IRIS Data Management Center. The facilities of the IRIS Consortium are supported by the National Science Foundation under Cooperative Agreement EAR-0552316, the NSF Office of Polar Programs and the DOE National Nuclear Security Administration.

References

Barker, S.E., and S.D. Malone (1991), Magmatic system geometry at Mount St. Helens modeled from the stress field associated with posteruptive earthquakes, *J. Geophys. Res.*, *96*(7), 11,883-11,894.

Bonaccorso, A., and P.M. Davis (1999), Models of ground deformation from vertical volcanic conduits with application to eruptions of Mount St. Helens and Mount Etna, *J. Geophys. Res.*, *104*(B5), 10,531-10,542.

Casadevall, T.J., W. Rose, and T. Gerlach (1983), Gas Emissions and the Eruptions of Mount St. Helens Through 1982, *Science*, *221*(4618), 1383 - 1385.

Castaño, S.S. (2002), The Lithosphere-Asthenosphere System Beneath Fennoscandia (Baltic Shield) by Body-Wave Tomography, Ph.D. thesis, 191 pp, Swiss Federal Institute of Technology, Zürich.

Chadwick, W.W., R. Archuleta, J., and D.A. Swanson (1988), The mechanics of ground deformation precursory to dome-building extrusions at Mount St. Helens 1981-1982 *J. Geophys. Res.*, *93*(B5), 4351-4366.

Christensen, N.I., and W.D. Mooney (1995), Seismic velocity structure and composition of the continental crust: a global view, *J. Geophys. Res.*, *100*(B7), 9761-9788.

Clynne, M.A., A.T. Calvert, E.W. Wolfe, R.C. Evarts, R.J. Fleck, and M.A. Lanphere (2008), The Pleistocene Eruptive History of Mount St. Helens, Washington - From 300,000 to 12,800 Years Ago, in *A Volcano Rekindled: The Renewed Eruption of Mount St. Helens, 2004-2006*, edited by D. R. Sherrod, W. E. Scott and P. H. Stauffer, U.S. Geol. Surv. 1750.

Eberhart-Phillips, D. (1990), Three-dimensional P and S velocity structure in the Coalinga region, California, *J. Geophys. Res.*, *95*(B10), 15,343-15,363.

Endo, E.T., D. Dzurisin, and D.A. Swanson (1990), Geophysical and observational constrains for the ascent rates of dacitic magma at Mount St. Helens, in *Magma Transport and Storage*, edited by M. P. Ryan, pp. 317-334, John Wiley & Sons, Chichester, UK.

Evans, J.R., and J.J. Zucca (1988), Active high-resolution seismic tomography of compressional wave velocity and attenuation structure at Medicine Lake Volcano, Northern California Cascade Range, *J. Geophys. Res.*, *93*(B12), 15,016-15,036.

Evans, J.R., D. Eberhart-Phillips, and C.H. Thurber (1994), User's manual for SIMULPS12 for imaging v_p and v_p/v_s: a derivative of the "Thurber" tomographic inversion SIMUL3 for local earthquakes and explosions, Open-File Rep., 101 pp, U.S. Geol. Surv., Reston, VA.

Evarts, R.C., R.P. Ashley, and J.G. Smith (1987), Geology of the Mount St. Helens area: Record of discontinuous volcanic and plutonic activity in the Cascade Arc of Southern Washington, *J. Geophys. Res.*, *92*(B10), 10,155-110,169.

Evarts, R.C., and R.P. Ashley (1990), Preliminary geologic map of the Goat Mountain quadrangle, Cowlitz County, Washington, Open-File Rep., 47 pp, U.S. Geol. Surv., Reston, VA.

Finn, C., and D.L. Williams (1987), An aeromagnetic study of Mount St. Helens, *J. Geophys. Res.*, *92*(B10), 10,194-110,206.

Hammond, W.C., and E.D. Humphreys (2000), Upper mantle seismic wave velocity: Effects of realistic partial melt geometries, *J. Geophys. Res.*, *105*, 10,975-910,986.

Haslinger, F., and E. Kissling (2001), Investigating effects of 3-D ray tracing methods in local earthquake tomography, *Phys. Earth Planet. Inter.*, *123*(103-114).

Kissling, E., W.L. Ellsworth, D. Eberhart-Phillips, and U. Kradolfer (1994), Initial reference models in local earthquake tomography, *J. Geophys. Res.*, *99*, 19,635–619,646.

Lees, J.M., and R.S. Crosson (1989), Tomographic inversion for three-dimensional velocity structure at Mount St. Helens using earthquake data, *J. Geophys. Res.*, *94*(B5), 5716-5728.

Lees, J.M., and R.S. Crosson (1990), Tomographic imaging of local earthquake delay times for three-dimensional velocity variation in Western Washington, *J. Geophys. Res.*, *95*(B4), 4763-4776.

Lees, J.M. (1992), The magma system of Mount St. Helens; non-linear high-resolution P-wave tomography, *J. Volcanol. Geotherm. Res.*, *53*, 103-116.

Malone, S.D., and G.L. Pavlis (1983), Velocity structure and relocation of earthquakes at Mount St. Helens, *Eos Trans. AGU*, *64*(45), Abstract, 895.

Mavko, G.M. (1980), Velocity and Attenuation in Partially Molten Rocks, *J. Geophys. Res.*, *85*(B10), 5173-5189.

Moran, S.C. (1994), Seismicity at Mount St. Helens, 1987-1992: Evidence for repressurization of an active magmatic system, *J. Geophys. Res.*, *99*(B3), 4341-4354, doi:4310.1029/4393JB02993.

Moran, S.C., J.M. Lees, and S.D. Malone (1999), P wave crustal velocity structure in the greater Mount Rainier area from local earthquake tomography, *J. Geophys. Res.*, *104*(5), 10,775 - 10,786.

Murase, T., and A.R. McBirney (1973), Properties of Some Common Igneous Rocks and Their Melts at High Temperatures, *Geol Soc Am Bull*, *84*(11), 3563-3592.

Musumeci, C., S. Gresta, and S.D. Malone (2002), Magma system recharge of Mount St. Helens from precise relative hypocenter location of microearthquakes, *J. Geophys. Res.*, *107*(B10), doi:10.1029/2001JB000629.

Pallister, J.S., R.P. Hoblitt, D.R. Crandell, and D.R. Mullineaux (1992), Mount St. Helens a decade after the 1980 eruptions: magmatic models, chemical cycles, and a revised hazards assessment, *Bull. Volcan.*, *54*(2), 126-146.

Pallister, J.S., C.R. Thornber, K.V. Cashman, M.A. Clynne, H.A. Lowers, C.W. Mandeville, I.K. Brownfield, and G.P. Meeker (2008), Petrology of the 2004-2006 Mount St. Helens lava dome-implications for magmatic plumbing and eruption triggering, in *A Volcano Rekindled: The Renewed Eruption of Mount St. Helens, 2004-2006*, edited by D. R. Sherrod, W. E. Scott and P. H. Stauffer, U.S. Geolog. Surv. Prof. Pap. 1750.

Parsons, T., R.E. Wells, M.A. Fisher, E. Flueh, and U.S. ten Brink (1999), Three-dimensional velocity structure of Siletzia and other accreted terranes in the Cascadia forearc of Washington, *J. Geophys. Res.*, *104*(B8), 18,015-18,039.

Rutherford, M.J., and J.D. Devine (2008), Magmatic conditions and processes in the storage zone of the 2004-2006 Mount St. Helens dacite, in *A Volcano Rekindled: The Renewed Eruption of Mount St. Helens, 2004-2006*, edited by D. R. Sherrod, W. E. Scott and P. H. Stauffer, U.S. Geolog. Surv. Prof. Pap. 1750.

Sato, H., I.S. Sacks, T. Murase, and C.M. Scarfe (1988), Thermal structure of the low velocity zone derived from laboratory and seismic investigaitons, *Geophys. Res. Lett., 15*(11), 1227-1230, doi.

Scandone, R., and S.D. Malone (1985), Magma supply, magma discharge and readjustment of the feeding system of mount St. Helens during 1980, *J. Volcanol. Geotherm. Res.*, *23*(3-4), 239-262, doi:210.1016/0377-0273(1085)90036-90038

Stanley, W.D., C. Finn, and J. Plesha, L. (1987), Tectonics and conductivity structures in the Southern Washington Cascades, *J. Geophys. Res.*, *92*(B10), 10,179-10,193.

Thurber, C.H. (1983), Earthquake locations and three-dimensional crustal structure in the Coyote Lake area, central California, *J. Geophys. Res.*, *88*(B10), 8226-8236.

Waite, G.P., R.B. Smith, and R.M. Allen (2006), V_P and V_S structure of the Yellowstone hot spot from teleseismic tomography: Evidence for an upper mantle plume, *J. Geophys. Res., 111*, B04303, doi:10.1029/2005JB003867.

Waite, G.P., B.A. Chouet, and P.B. Dawson (2008), Eruption dynamics at Mount St. Helens imaged from inversion of broadband waveforms: interaction of the shallow magmatic and hydrothermal system, *J. Geophys. Res., 113*, B02305, doi:10.1029/2005JB005259.

Walsh, T.J., M.A. Korosec, W.M. Phillips, R.L. Logan, and H.W. Schasse (1987), Geologic map of Washington - southwest quadrant, Washington Division of Geology and Earth Resources.

Weaver, C.S., and S.W. Smith (1983), Regional tectonic and earthquake hazard implications of a crustal fault zone in southwestern Washington, *J. Geophys. Res.*, *88*, 10,371-10,383.

Weaver, C.S., W.C. Grant, and J. Shemeta, E. (1987), Local crustal extension at Mount St. Helens, Washington, *J. Geophys. Res.*, *92*(B10), 10,170-10,178.

Wiemer, S., and S.R. McNutt (1997), Variations in the frequency-magnitude distribution with depth in two volcanic areas; Mount St. Helens, Washington, and Mt. Spurr, Alaska, *Geophys. Res. Lett.*, *24*(2), 189-192.

3. Figure captions

Figure 1. Station location map shows the temporary broadband stations (dark diamonds) and a subset of the permanent network stations (light circles and diamond) plotted on topography contoured at 200 m intervals. Station STD was the only permanent broadband station running during the temporary deployment. Inset in the upper left corner shows the location of Mount St. Helens in southern Washington. Inset in the lower right corner shows a close up of the crater stations plotted on topography contoured at 40 m intervals. Spirit Lake, the St Helens Seismic Zone (SHZ) and the approximate locations of the Spud Mountain and Spirit Lake Plutons are also shown.

Figure 2. The open circles indicate all 12,454 earthquakes in the PNSN catalog from March 1980 through June 2004, plus selected events from July 2005 to January 2006 recorded in the Mount St. Helens region. Black circles show only the 7,798 best-located events. These earthquakes have a gap $< 180^{o}$, 10 or more picks, nearest station within 1 focal depth, and RMS < 0.25 s. There is no vertical exaggeration.

Figure 3. The lines represent one-dimensional velocity models from which the 3-D models were derived. See the text for a description of the models.

Figure 4. Ray tracing for a shallow earthquake recorded on the flanks of MSH using our modified version of SIMULPS14 that uses topographic data to ensure rays stay in the Earth. The ray shooting (dotted) method typically finds less arcuate, shorter traveltime paths than the pseudo-bending (dashed) ray tracing method. Note that in the cross-sections some rays appear to be in the air; this is because all the ray paths are plotted, and the topography varies widely with azimuth. There is no vertical exaggeration.

Figure 5. Horizontal and vertical sliced through the multimodel average coarse-grid model are plotted as percent deviations from the starting model (color) and contoured with the absolute velocity. The plots are faded where resolution is poor (diagonal element of the resolution matrix less than 0.15). White lines outline regions with minimal trade-off between adjacent nodes, which are plotted as red plus signs (spread value less than 1). There is no vertical exaggeration.

Figure 6. Horizontal and vertical sliced through the multimodel average fine-grid model are plotted as percent deviations from the starting model (color) and contoured with the absolute velocity. The plots are faded where resolution is poor (diagonal element of the resolution matrix less than 0.15). White lines outline regions with minimal trade-off between adjacent nodes, which are plotted as red plus signs (spread value less than 1.15). There is no vertical exaggeration.

Figure 7. A west-east cross section through a single fine-grid model highlights the low velocity anomaly directly beneath the volcano. There is no vertical exaggeration.

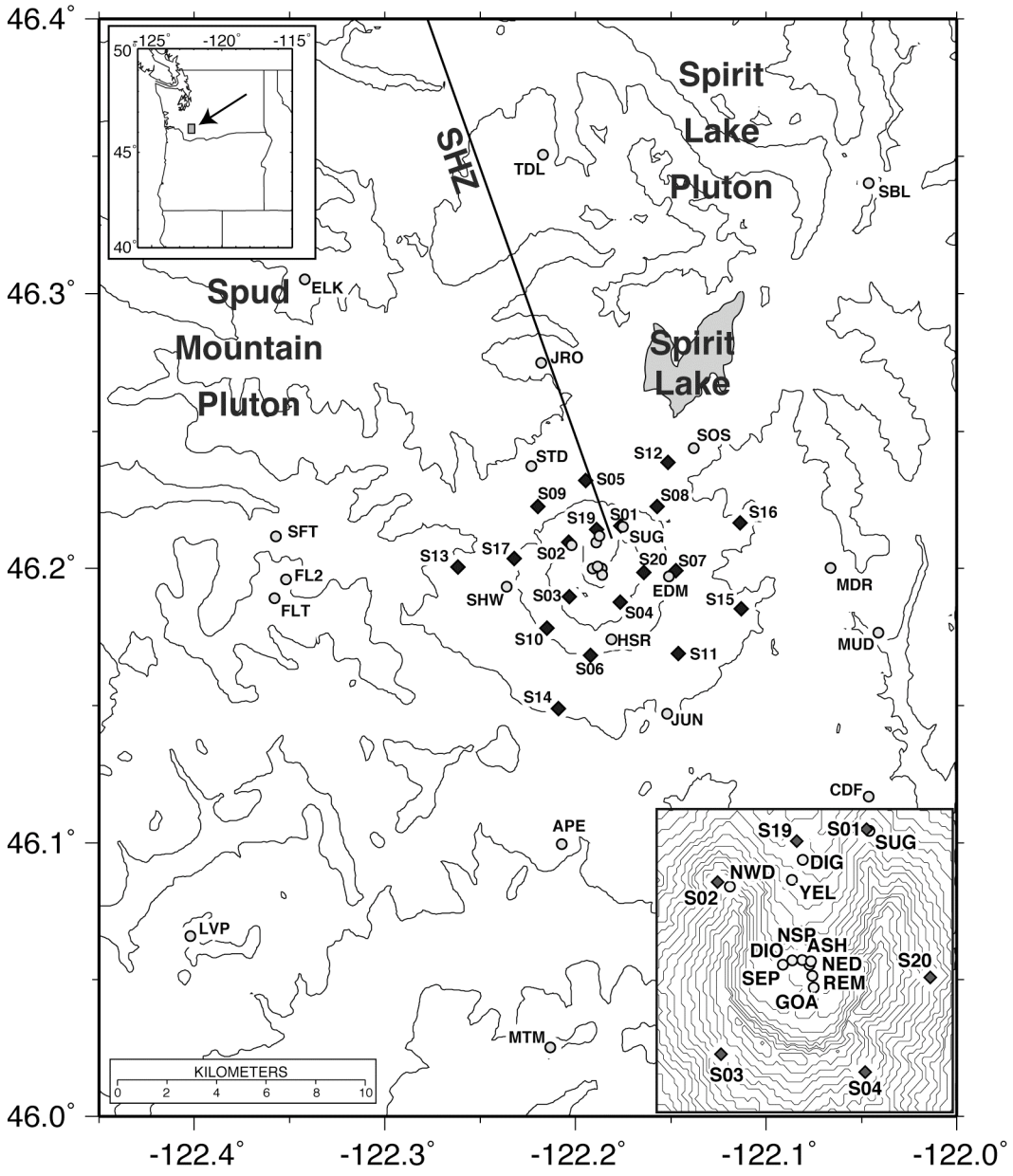
Spirit
Lake
Pluton
SHZ
TDL
SBL
Spud
Mountain
Pluton
ELK
JRO
Spirit
Lake
SOS
STD
S12
S05
S09
S08
S19
S01
S16
SUG
SFT
S13
S17
S02
S20
S07
FL2
EDM
MDR
SHW
S03
S15
FLT
S04
S10
HSR
S11
MUD
S06
S14
JUN
CDF
APE
S19
S01
SUG
DIG
NWD
S02
YEL
LVP
NSP
ASH
DIO
NED
S20
SEP
REM
GOA
MTM
S03
S04
KILOMETERS
0 2 4 6 8 10
46.4˚
46.3˚
46.2˚
46.1˚
46.0˚
-122.4˚
-122.3˚
-122.2˚
-122.1˚
-122.0˚
125˚
120˚
115˚
50˚
45˚
40˚

Figure 1.

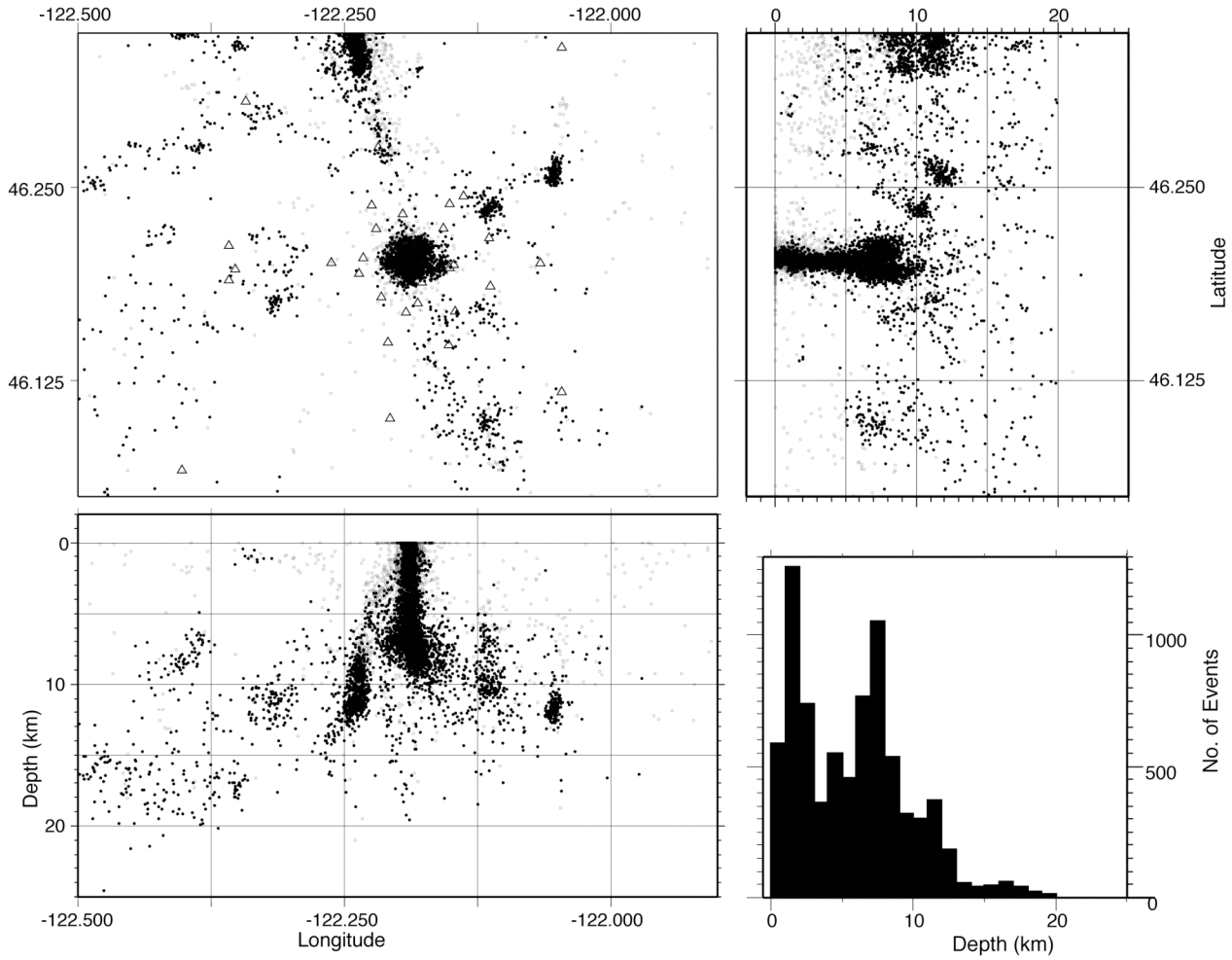
-122.500
-122.250
-122.000
46.250
46.125
0
10
20
Latitude
Depth (km)
Longitude
No. of Events
1000
500
0

Figure 2.

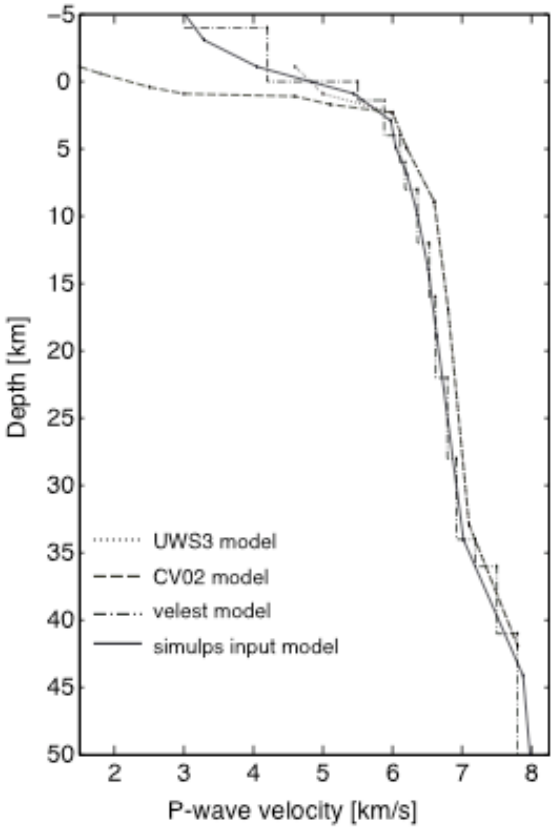
Depth [km]
P-wave velocity [km/s]
UWS3 model
CV02 model
velest model
simulps input model

Figure 3.

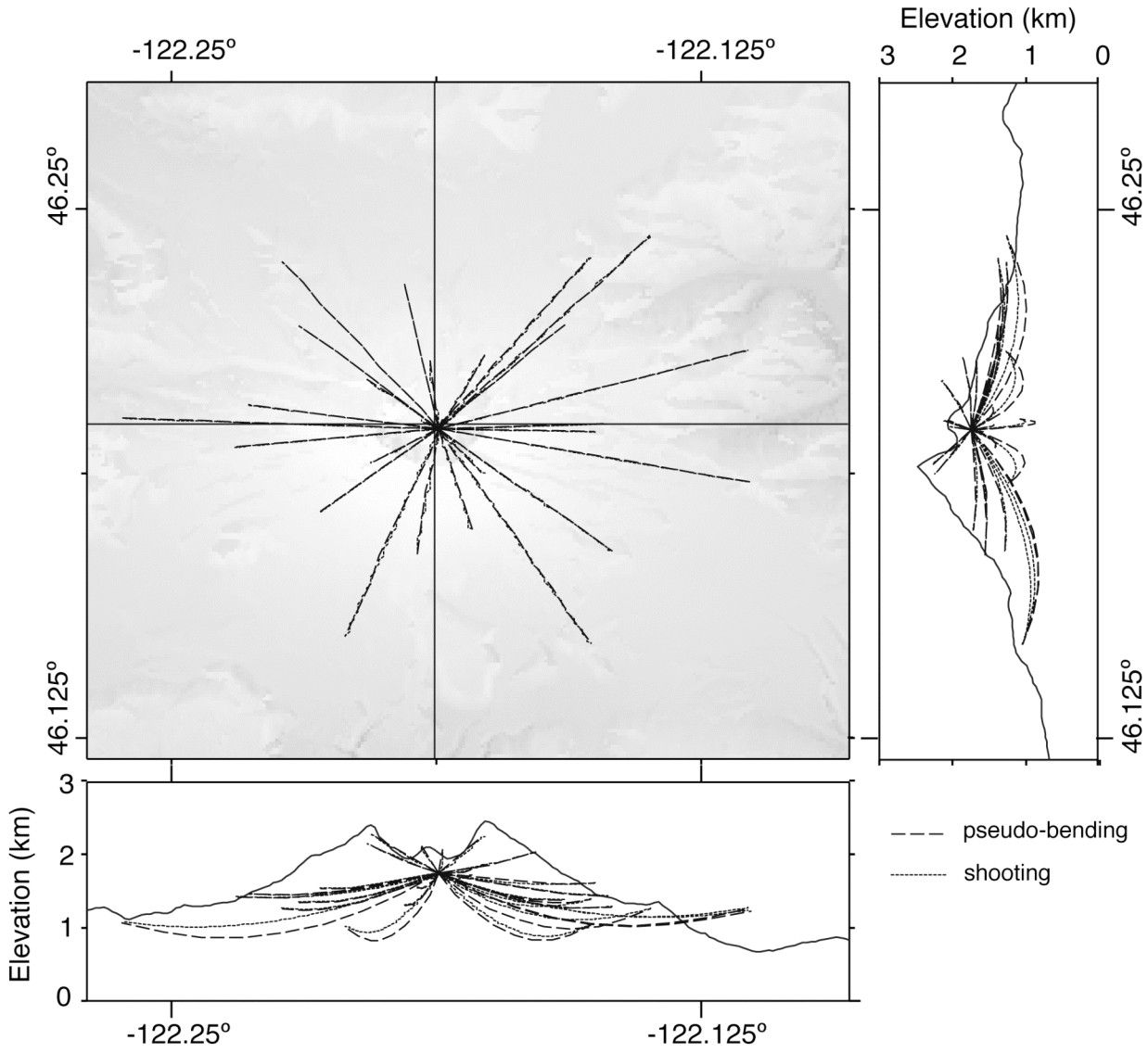
Elevation (km)
3
2
1
0
-122.25°
-122.125°
46.25°
46.125°
Elevation (km)
3
2
1
0
-122.25°
-122.125°
pseudo-bending
shooting

Figure 4.

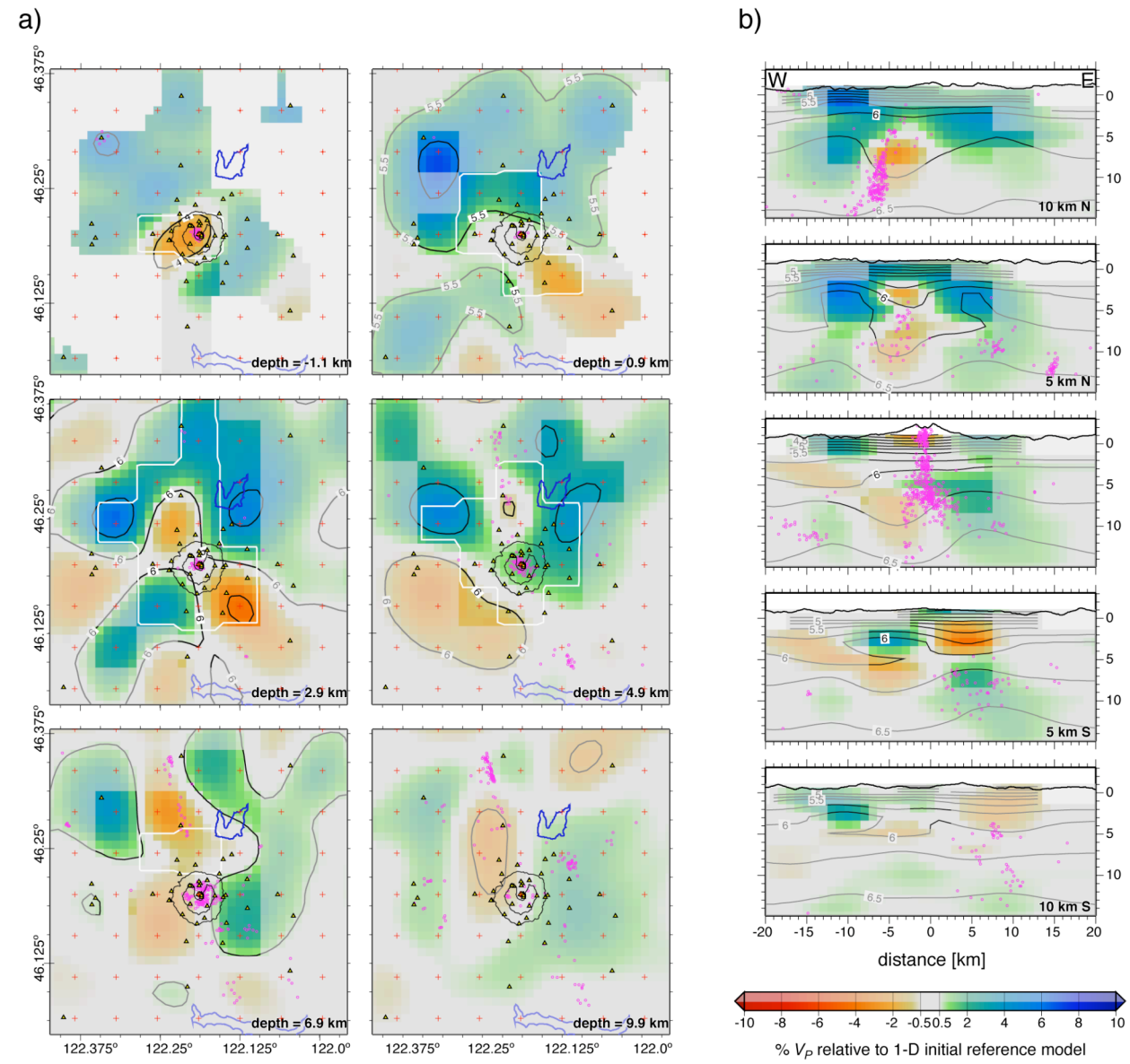
a)
b)
depth = 1.1 km
depth = 0.9 km
depth = 2.9 km
depth = 4.9 km
depth = 6.9 km
depth = 9.9 km
46.375°
46.25°
46.125°
122.375°
122.25°
122.125°
122.0°
W
E
10 km N
5 km N
5 km S
10 km S
distance [km]
% V_P relative to 1-D initial reference model

Figure 5.

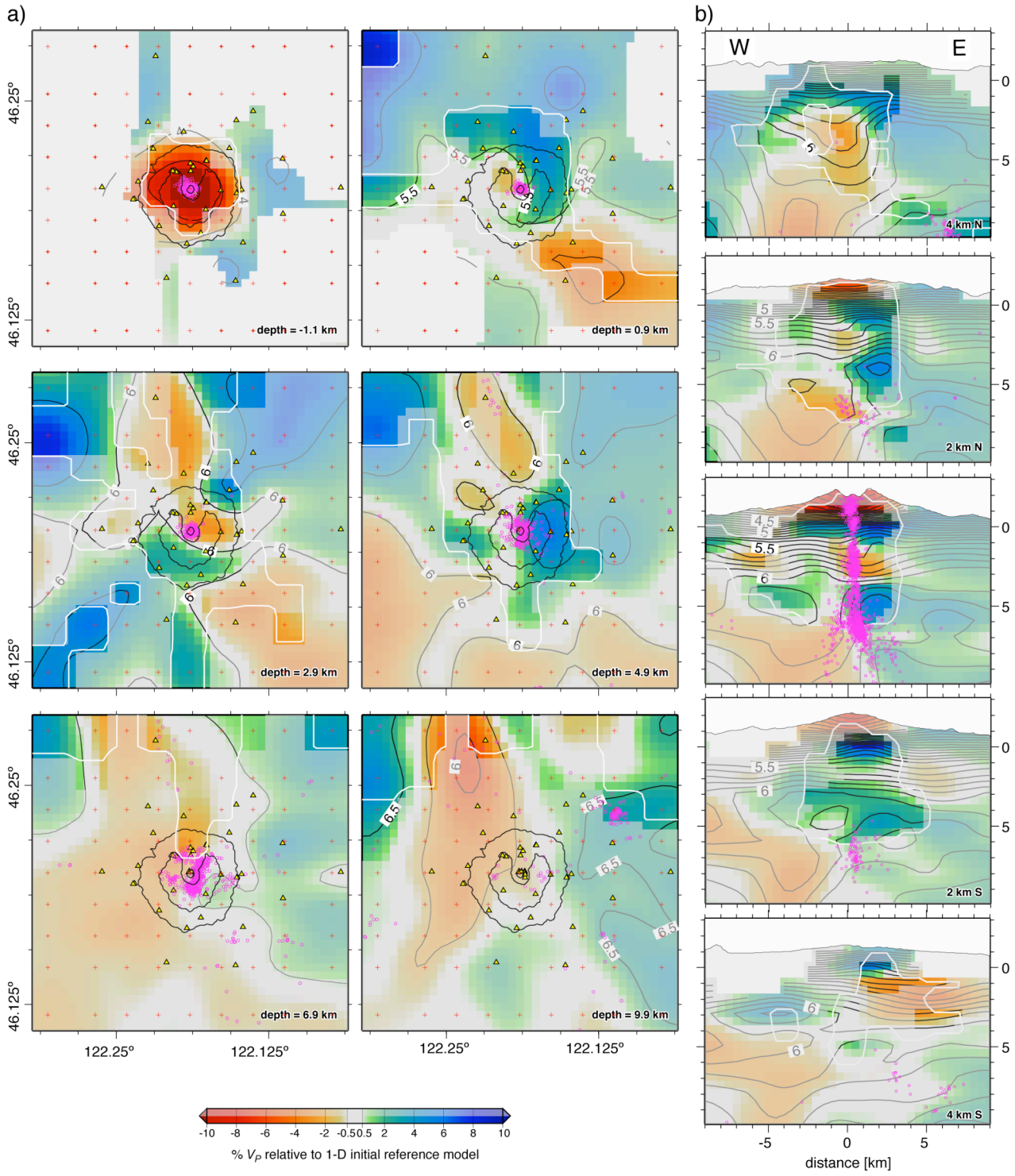
a)
b)
W
E
depth = -1.1 km
depth = 0.9 km
depth = 2.9 km
depth = 4.9 km
depth = 6.9 km
depth = 9.9 km
46.25°
46.125°
122.25°
122.125°
4 km N
2 km N
2 km S
4 km S
distance [km]
% V_P relative to 1-D initial reference model

Figure 6.

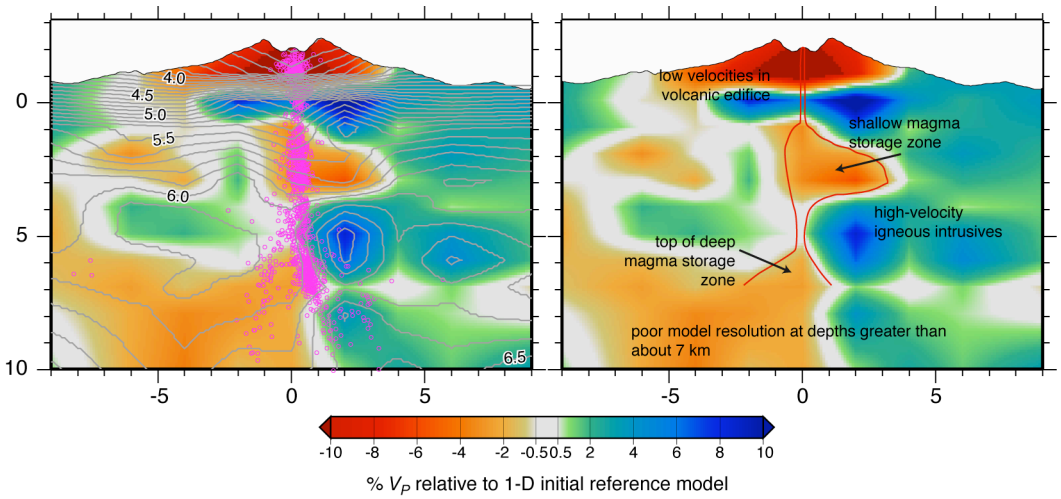
4.0
4.5
5.0
5.5
6.0
6.5
0
5
10
-5
0
5
low velocities in volcanic edifice
shallow magma storage zone
high-velocity igneous intrusives
top of deep magma storage zone
poor model resolution at depths greater than about 7 km
-10 -8 -6 -4 -2 -0.5 0.5 2 4 6 8 10
% V_P relative to 1-D initial reference model

Figure 7.

Supplementary Material

Supplementary figures and tables are provided to offer the reader additional information about the details of tomographic models. The figures and tables are discussed in the text.

Figure S1. Horizontal slices through the coarse-grid synthetic checkerboard model derived from the average of 25 offset models are plotted in (a) and horizontal slices through the resolution matrix of one of the models are plotted in (b), as described in the text. In (a) the input synthetic anomalies are outlined with red and blue boxes. In both (a) and (b), the node positions from one of the 25 models are plotted as black squares, stations are plotted as triangles, the 1500 and 2000 m elevation contours around Mount St. Helens are plotted in black, the outline of Spirit Lake is shown in blue, and earthquakes are plotted as pink circles. In (b) the background color corresponds to the spread value of the given node and the size and color of the circle corresponds to the value of the diagonal element of the resolution matrix. The red lines represent the extent of significant smearing by poorly resolved nodes. This was quantified by examining the off-diagonal components of the resolution matrix; if one or more off-diagonal elements had a value greater than or equal to 70% of the diagonal component, it was considered to trade-off with the node significantly. The red lines contour the 70% of the value of the diagonal component, after interpolating to 1 km.

Figure S2. The 12 sections are horizontal slices through the fine-grid synthetic checkerboard model derived from the average of 16 offset models as described in the text. The input synthetic anomalies are outlined with red and blue boxes. The node positions from one of the 16 models are plotted as black squares, stations are plotted as triangles, the 1500 and 2000 m elevation contours around Mount St. Helens are plotted in black, the outline of Spirit Lake is shown in blue, and earthquakes are plotted as pink circles.

Figure S3. The 12 sections are horizontal slices through the fine-grid resolution matrix as described in the text. The background color corresponds to the spread value of the given node and the size and color of the circle corresponds to the value of the diagonal element of the resolution matrix. The red lines represent the extent of significant smearing by poorly resolved nodes. This was quantified by examining the off-diagonal components of the resolution matrix; if one or more off-diagonal elements had a value greater than or equal to 70% of the diagonal component, it was considered to trade-off with the node significantly. The red lines contour the 70% of the value of the diagonal component, after interpolating to 0.1 km. Stations are plotted as triangles, the 1500 and 2000 m elevation contours around Mount St. Helens are plotted in black, the outline of Spirit Lake is shown in blue, and earthquakes are plotted as pink circles.

Supplementary Table 1. Differences between 25 coarse-grid models calculated with shifted grids. The maximum difference represents the largest range of modeled velocities at any one point in the averaging grid. The standard deviation statistics for each layer are based on these ranges. Only the best-resolved nodes were used in this statistic to avoid artificially lowering the standard deviations.

Supplementary Table 2. Differences between 16 fine-grid models calculated with shifted grids. The data are presented as in Table 1.

Supplementary Table 3. Differences between two fine-grid models computed from independent data sets. The data are presented as in supplementary Tables 1 and 2

Table T1. Differences between 25 coarse-grid models calculated with shifted grids

Layer depth [km]	Reference Velocity [km/s]	Maximum range [km/s]	Maximum range [%]	Standard deviation [km/s]	Standard deviation [%]
-3.10	3.29	0.09	2.75%	0.01	0.37%
-1.10	4.05	0.37	9.11%	0.08	1.90%
0.90	5.44	0.30	5.60%	0.06	1.09%
2.90	5.98	0.54	9.02%	0.11	1.76%
4.90	6.05	0.27	4.47%	0.05	0.79%
6.90	6.21	0.44	7.08%	0.09	1.41%
9.90	6.36	0.23	3.59%	0.04	0.58%
13.90	6.51	0.21	3.19%	0.03	0.53%

Table T2. Differences between 16 fine-grid models calculated with shifted grids

Layer depth [km]	Reference Velocity [km/s]	Maximum range [km/s]	Maximum range [%]	Standard deviation [km/s]	Standard deviation [%]
-3.1	3.29	0.01	0.38%	0.00	0.09%
-2.1	3.67	0.17	4.57%	0.02	0.54%
-1.1	4.05	0.26	6.30%	0.04	1.08%
-0.1	4.75	0.29	6.05%	0.06	1.29%
0.9	5.44	0.27	4.96%	0.05	0.93%
1.9	5.71	0.38	6.70%	0.05	0.86%
2.9	5.98	0.41	6.89%	0.05	0.92%
3.9	6.01	0.34	5.58%	0.04	0.70%
4.9	6.05	0.29	4.72%	0.04	0.65%
5.9	6.13	0.36	5.95%	0.04	0.71%
6.9	6.21	0.19	2.98%	0.03	0.47%
7.9	6.26	0.17	2.79%	0.03	0.41%
9.9	6.36	0.20	3.07%	0.03	0.42%
13.9	6.51	0.14	2.19%	0.02	0.34%

Table T3. Differences between two fine-grid models calculated with independent data sets

Layer depth [km]	Reference Velocity [km/s]	Maximum range [km/s]	Maximum range [%]	Standard deviation [km/s]	Standard deviation [%]
-3.1	3.29	0.00	0.00%	0.00	0.00%
-2.1	3.67	0.03	0.82%	0.00	0.10%
-1.1	4.05	0.05	1.24%	0.01	0.24%
-0.1	4.75	0.13	2.74%	0.02	0.38%
0.9	5.44	0.13	2.39%	0.02	0.42%
1.9	5.71	0.13	2.28%	0.03	0.44%
2.9	5.98	0.10	1.67%	0.02	0.31%
3.9	6.01	0.14	2.33%	0.02	0.40%
4.9	6.05	0.13	2.15%	0.03	0.49%
5.9	6.13	0.11	1.79%	0.03	0.45%
6.9	6.21	0.11	1.77%	0.02	0.38%
7.9	6.26	0.17	2.72%	0.03	0.51%
9.9	6.36	0.19	2.99%	0.03	0.52%
13.9	6.51	0.13	2.00%	0.02	0.35%

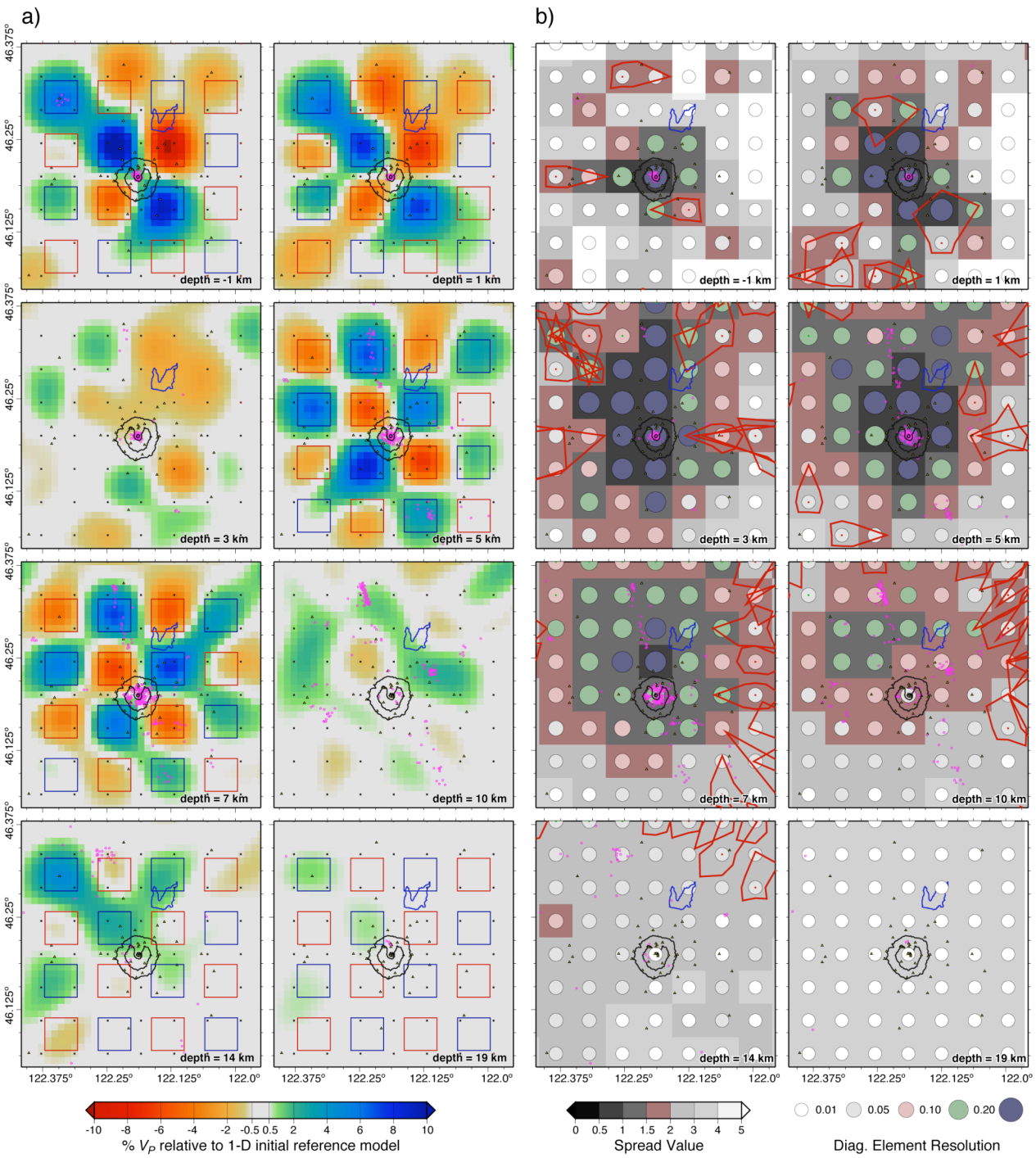

Supplementary Figure S1.

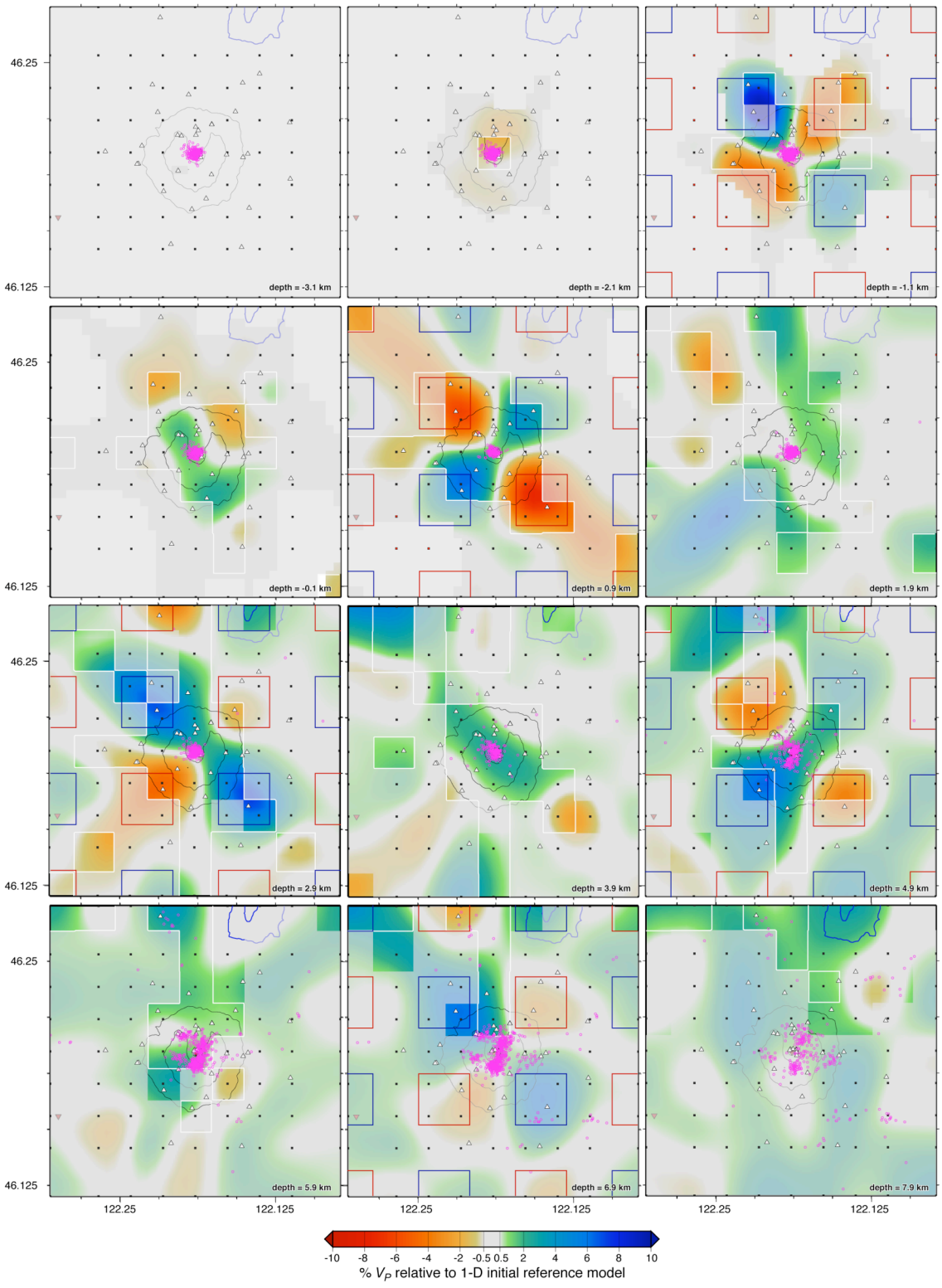

Supplementary Figure S3.

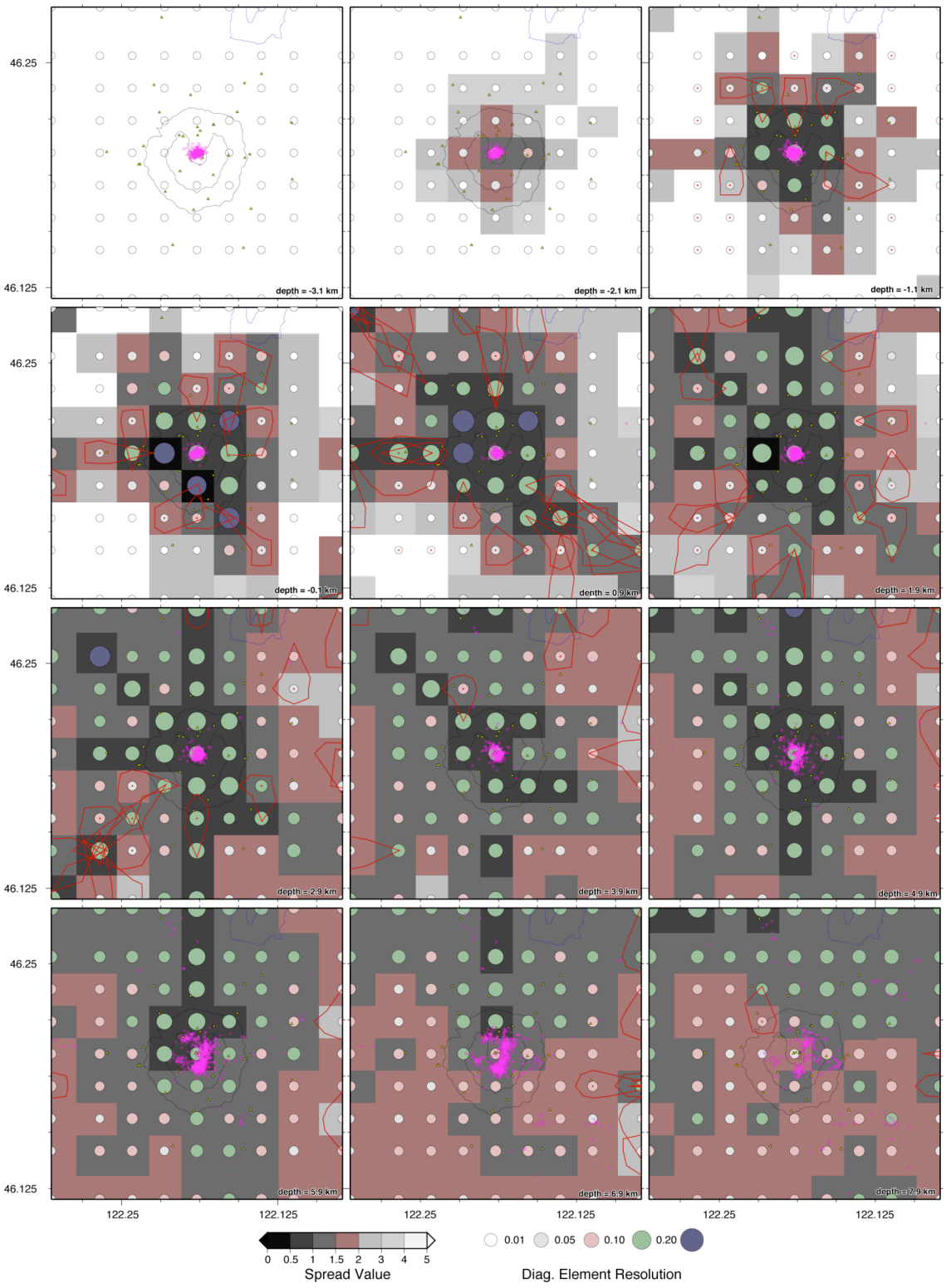

Supplementary Figure S3.